
Article:
Ball, J.E. orcid.org/0000-0003-4795-4007, Wild, J.M. orcid.org/0000-0002-7246-8660 and Norquay, G. orcid.org/0000-0002-4108-9035 (2024) Evaluating modeling approaches for Rb-129Xe spin-exchange optical pumping and the effect of Rb vapor density heterogeneity. Journal of Applied Physics, 136 (24). 243104. ISSN 0021-8979

https://doi.org/10.1063/5.0233678

Journal of Applied Physics

RESEARCH ARTICLE | DECEMBER 24 2024

Evaluating modeling approaches for Rb-^{129}Xe spin-exchange optical pumping and the effect of Rb vapor density heterogeneity

J. E. Ball ; J. M. Wild ; G. Norquay

J. Appl. Phys. 136, 243104 (2024)
https://doi.org/10.1063/5.0233678

Journal of Applied Physics ARTICLE pubs.aip.org/aip/jap

Evaluating modeling approaches for Rb-^{129}Xe spin-exchange optical pumping and the effect of Rb vapor density heterogeneity

Cite as: J. Appl. Phys. **136**, 243104 (2024); doi: 10.1063/5.0233678
Submitted: 16 August 2024 · Accepted: 7 December 2024 ·
Published Online: 24 December 2024

J. E. Ball, J. M. Wild, and G. Norquay[a)]

AFFILIATIONS

POLARIS, Division of Clinical Medicine, School of Medicine and Population Health, The University of Sheffield, Sheffield, United Kingdom

[a)]**Author to whom correspondence should be addressed:** g.norquay@sheffield.ac.uk

ABSTRACT

The applicability of commonly used ^{129}Xe nuclear polarization (P_{Xe}) buildup models to large optical cell polarizers, which operate at lower gas pressures when compared to small cell polarizers for which spin-exchange optical pumping (SEOP) models were originally developed, has yet to be systematically evaluated. In addition, spatial heterogeneity of Rb vapor density ([Rb]) and its impact on SEOP in low pressure, large optical cell polarizers remains poorly understood. In this theoretical study, it was shown that 1D analytical and numerical P_{Xe} buildup models yield diverging P_{Xe} and critical flow rate values at low flow rates and high laser absorption, contributing to the discrepancy between theoretical and experimentally measured production rates. Additionally, it was found that [Rb] heterogeneity leads to lower P_{Xe} buildup and an undesirable increase in optimal cell temperature, while the optimal laser absorption remains relatively unchanged. The updated simulation framework presented here can be utilized to model other SEOP systems.

I. INTRODUCTION

Hyperpolarized (HP) xenon-129 (^{129}Xe) has applications in various fields such as lung MRI studies,[1,2] biosensors,[3–5] material science,[6] and non-standard model physics exploration.[7] The most common technique for producing large quantities of HP-^{129}Xe is spin-exchange optical pumping (SEOP),[8] where an alkali metal [most commonly rubidium (Rb)] is irradiated with circularly polarized light in a magnetic field to create high Rb electronic polarization. Collisional interactions between Rb and ^{129}Xe mediate transfer of angular momentum to ^{129}Xe nuclei, resulting in high ^{129}Xe nuclear polarization (P_{Xe}) and high detection sensitivity in NMR and MRI.

The two commonly used methods of SEOP polarizer operation are termed batch-mode[9] and continuous-flow (CF) mode.[10] Batch-mode employs low temperature (up to 80 °C[11–13]) and high Xe densities (up to 90%[11–13]), to achieve high P_{Xe} doses, without the need to separate Xe from the gas mixture. CF mode involves continuous Xe flow through the optical cell, necessitating lean Xe gas mixtures (1%–3%) and higher temperatures for efficient spin exchange. Xe in the exiting gas mixture is then cryogenically separated from the buffer gases in order to produce a high concentration Xe dose. CF setups typically utilize narrow linewidth lasers ($\Delta\lambda_l < 1$ nm) and large volume optical cells ($V_{cell} \geq 1$ L[14–17]) at low gas pressures, where spin-exchange efficiency is highest due to the increased fraction of exchange with van der Waals (vdW) molecules,[18,19] leading to higher production rates than observed on small cell polarizers operating at high gas pressures. See Refs. 10, 20, and 21 and Refs. 14–17 for examples of small- and large-cell CF polarizers, respectively.

Accurate P_{Xe} buildup models are used to aid multi-parametric optimization of SEOP polarizer performance. Different P_{Xe} buildup models, both numerical[15,22,23] and analytical,[10,16,17,20,21] have been used in simulations, which rely on different assumptions of gas transport in the optical cell. Analytical models have been most commonly implemented, due to their simplicity and assumed applicability to small cell setups, based on the small geometry and historically slow flow rates. Numerical models have been used in 3D simulations[23–26] and we hypothesized that these models are more applicable than analytical models for large optical cell setups

operating at high flow rates and low cell pressures. In addition, modeling simplified optical pumping rate attenuation,[27,28] where the optical pumping photon flux is assumed to remain spectrally Gaussian with attenuation due to absorption by the Rb vapor along the length of the optical cell, has been used in Refs. 23, 16, 25, 29, and 17, though the validity of this simplification remains uncertain for all polarizer operating conditions. Discrepancy between modeled and experimentally measured polarizer performance exists, and improper implementation of P_{Xe} buildup models could be a contributing factor.

This work aims to evaluate the utility of these models to P_{Xe} buildup in a high-throughput CF polarizer, using a revised modeling framework that considers gas composition dependent molecular lifetime regimes and Rb polarization dependence in Rb spin-destruction and Rb-^{129}Xe spin-exchange, which was highlighted by Kelley and Branca[30] and is not considered in previous simulation work.[16,20,21,23] We also explored the effect of heterogeneous in-cell Rb vapor density ([Rb]) distributions, which have been measured in our CF polarizer previously.[31]

II. MODEL FRAMEWORK

This section presents a revised model framework used in this work to simulate SEOP in CF polarizers. This adaptable framework can also be applied to simulate other CF and batch-mode polarizers.

A. Optical pumping

Steady-state Rb electronic polarization is defined as

$$P_{Rb}(z) = \frac{R(z)}{R(z) + \Gamma_{SD}(P_{Rb})}, \tag{1}$$

where R is the optical pumping rate (photon absorption rate at zero P_{Rb}) and Γ_{SD} is the Rb electronic spin-destruction rate, which vary with longitudinal optical cell position (z). R is related to the circularly polarized resonant photon flux (Φ) and the absorption cross section for unpolarized light (σ_s) by[32]

$$R(z) = \int \Phi(\nu, z)\sigma_s(\nu)\mathrm{d}\nu. \tag{2}$$

σ_s typically has a Lorentzian spectral profile $L(\nu)$[32] and Φ has an initial Gaussian spectral profile $G(\nu)$ before attenuation along z is considered,

$$\sigma_s(\nu) = \sigma_0 L(\nu) = \pi r_0 c f \frac{\Delta\nu_a/2\pi}{(\nu - \nu_a)^2 + \left(\frac{\Delta\nu_a}{2}\right)^2}, \tag{3}$$

where $\sigma_0 = \int \sigma_s \mathrm{d}\nu = \pi r_0 c f$, r_0 is the classical electron radius, c is the speed of light, f is the D_1 absorption oscillator strength, $\Delta\nu_a = \sum_i [\mathrm{G}]_i (\Delta\nu_a)_i$ is the absorption linewidth, and $\nu_a = \nu_{D_1} + \sum_i [\mathrm{G}]_i (\nu_a)_i$ is the absorption center frequency, which are broadened and shifted by the presence of each gas species i, respectively.[33] ν_{D_1} is the non-shifted absorption center frequency.

The initial photon flux is given by

$$\Phi(\nu, 0) = \Phi(0)G(\nu) = \frac{P_l n_p}{A}\frac{2}{\Delta\nu_l}\sqrt{\frac{\ln 2}{\pi}}\exp\left[-4\ln 2\left(\frac{(\nu - \nu_l)}{\Delta\nu_l}\right)^2\right], \tag{4}$$

where $\Phi(0) = \frac{P_l n_p}{A}$, P_l is the laser power, A is the beam area, n_p is the number of photons per Joule at the pump laser center wavelength λ_l, $\Delta\nu_l$ is the laser full width at half maximum (FWHM), and ν_l is the laser center frequency.

1. Photon attenuation

The photon flux incident on a sample will be attenuated by absorption and lead to decreasing flux penetrating into the Rb vapor sample within the optical cell.

Attenuation of Φ along z is described by[32]

$$\frac{\mathrm{d}\Phi(\nu, z)}{\mathrm{d}z} = -\lambda_{\sigma_+}^{-1}\Phi(\nu, z) = -[\mathrm{Rb}]\sigma_s(\nu)(1 - P_{Rb}(z))\Phi(\nu, z). \tag{5}$$

where $\lambda_{\sigma_+}^{-1}$ is the mean absorption length per circularly polarized photon.

Laser (or photon) absorption, which is the proportion of photon flux absorbed across the full optical cell length L_{cell} is

$$\delta\Phi = \frac{\Phi(0) - \Phi(L_{cell})}{\Phi(0)} \times 100\%. \tag{6}$$

2. Optical pumping rate attenuation

Alternatively, a directly proportional relationship between R and Φ can be assumed in order to simplify modeling optical pumping rate attenuation. The coefficient relating the photon flux to R has previously been shown to be[27,34]

$$\alpha = \frac{R}{\Phi} = \frac{2\sqrt{\pi \ln 2} r_e f_{D_1} \lambda_l^3 w'(r, s)}{hc\Delta\lambda_l n_p}, \tag{7}$$

where $\Delta\lambda_l$ is the pump laser linewidth. $w'(r, s)$ is the real part of the complex overlap function (w) given by $w = w' + iw''$ $= e^{[\ln 2(r+is)^2]}\mathrm{erfc}\left(\sqrt{\ln 2}[r + is]\right)$. Here, $s = 2(\nu_l - \nu_a)/\Delta\nu_l$ is the relative detuning and $r = \Delta\nu_a/\Delta\nu_l$ is the relative atomic linewidth of the atomic absorption line to the laser spectral output. If we assume that Φ remains spectrally Gaussian with attenuation, which is valid when the linewidths of the absorption cross section (σ_s) and laser profile ($\Phi(\nu, 0)$) are similar, then attenuation of R along z can be described by[28]

$$\frac{\mathrm{d}R(z)}{\mathrm{d}z} = -[\mathrm{Rb}]\alpha(1 - P_{Rb}(z))R(z). \tag{8}$$

For constant [Rb] along the cell length, Eq. (8) can be simplified to the explicit solution,[16]

$$R(z) = \Gamma_{SD} W\left(e^{(k-\alpha[\mathrm{Rb}]z)}/\Gamma_{SD}\right), \tag{9}$$

where $k = \ln(R_0) + R_0/\Gamma_{SD}$[28] and W is the Lambert W function ($f(x) = xe^x$, $W(f(x)) = x$).

Using $R = \alpha\Phi$ and Eq. (6), laser absorption can be calculated as

$$\delta\Phi = \frac{R(0) - R(L_{cell})}{R(0)} \times 100\%. \tag{10}$$

Comparison of the optical pumping and photon flux attenuation models is presented in this work.

3. Rb spin-destruction rate

Rb electronic spin-destruction occurs due to both S-damping, which is not affected by Rb nuclear spin due to the short interaction times, and F-damping, which is affected by Rb nuclear spin due to the relatively long interaction times.[19] S-damping has contributions from both binary and vdW interactions, while F-damping is solely due to vdW interactions. Rb electronic spin-destruction rate, Γ_{SD} is[34]

$$\Gamma_{SD}(P_{Rb}) = \frac{1}{T_S^{bc}} + \Gamma_{SD}^{vdW}(P_{Rb}) = \frac{1}{T_S^{bc}} + \sum_i \eta_i \left[\frac{1}{T_{S,i}^{vdW}} + \frac{v_i(P_{Rb})}{T_{F,i}}\right], \tag{11}$$

for $i \in \{^{85}\mathrm{Rb}, ^{87}\mathrm{Rb}\}$, where η_i is the abundance of the Rb isotope i, $\frac{1}{T_S^{bc}}$, $\frac{1}{T_S^{vdW}}$, and $\frac{1}{T_F}$ are the S binary, S vdW, and F damping rates, respectively. $v(P_{Rb})$ is the coefficient that accounts for relaxation in long lived vdW molecules given by

$$v(P_{Rb}) = \frac{q(I, P_{Rb})}{[I]^2}, \tag{12}$$

where $[I] = 2I + 1$ is the statistical weight of the Rb nuclear spin quantum number I and $q(I, P_{Rb}) = 1 + \varepsilon(I_i, P_{Rb})$ is the paramagnetic coefficient for P_{Rb} within a spin-temperature distribution. The q values for ^{87}Rb ($I = 3/2$) and ^{85}Rb ($I = 5/2$) isotopes are given by[34]

$$1 + \varepsilon\left(\frac{3}{2}, P_{Rb}\right) = 1 + \frac{5 + P_{Rb}^2}{1 + P_{Rb}^2}, \tag{13}$$

$$1 + \varepsilon\left(\frac{5}{2}, P_{Rb}\right) = 1 + \frac{35 + 42P_{Rb}^2 + 3P_{Rb}^4}{3 + 10P_{Rb}^2 + 3P_{Rb}^4}. \tag{14}$$

The binary S-damping Rb spin destruction rate is

$$\frac{1}{T_S^{bc}} = \eta_K[\mathrm{Xe}]\langle v\sigma_{KS}\rangle + [\mathrm{Rb}]\langle v\sigma_{SS}\rangle + \sum_j [\mathrm{G}]_j\langle v\sigma_{NS}\rangle_j, \tag{15}$$

for any gas density composition $j \in \{\mathrm{Xe}, \mathrm{N_2}, \mathrm{He}\}$, where $[\mathrm{G}]_j$ is the gas number density, $\langle v\sigma_{NS}\rangle_i$ is the rate coefficient for binary Rb and i gas collisions, $\langle v\sigma_{KS}\rangle$ is the rate coefficient for Rb-^{129}Xe spin-exchange interactions during binary collisions, $\langle v\sigma_{SS}\rangle$ is the rate coefficient of Rb-Rb binary collisions, and η_K is the ^{129}Xe abundance. Gas composition dependent expressions for $\langle v\sigma_{NS}\rangle_i$, $\langle v\sigma_{KS}\rangle$, and $\langle v\sigma_{SS}\rangle$ are given in Table I.

The vdW S-damping Rb spin destruction rate is

$$\frac{1}{T_{S,i}^{vdW}} = \frac{C_{\alpha\gamma}}{T_{vW,A}} f_{S,i}, \tag{16}$$

where the three-body formation rate per Rb atom ($\frac{1}{T_{vW,A}}$) is defined as

$$\frac{1}{T_{vW,A}} = \frac{K_c[\mathrm{Xe}]}{\tau}, \tag{17}$$

where K_c is the molecular chemical equilibrium constant.[35] τ is the molecular lifetime defined by[16]

$$\tau = \frac{\phi_\gamma}{\omega}, \tag{18}$$

where $\omega = \gamma N/\hbar$ is the spin-rotation frequency of the Rb electron spin vector $\mathbf{S}$ about the rotational angular momentum vector $\mathbf{N}$ of the RbXe molecule. ϕ_γ is the phase angle subtended by $\mathbf{S}$ around $\mathbf{N}$ within a molecular lifetime τ, given by

$$\phi_\gamma = \sum_j \frac{[\mathrm{G}]_{0,j}}{[\mathrm{G}]_j}, \tag{19}$$

where $[\mathrm{G}]_{0,j}$ is defined as the characteristic third-body density for which the molecular breakup rate τ^{-1} is equal to ω. γ denotes the coupling constant that determines the strength of the spin-rotation interaction $\gamma\mathbf{N}\cdot\mathbf{S}$,[19]

$$C_{\alpha\gamma} = \frac{\eta_K\phi_\alpha^2}{2} + \frac{2\phi_\gamma^2}{3} \tag{20}$$

is a coefficient defined by the phase evolution angles for the vdW molecules ϕ_γ and $\phi_\alpha = \phi_\gamma/x$ (ϕ_α is phase precession angle of $\mathbf{S}$ around the ^{129}Xe nuclear spin $\mathbf{K}$), where x is the Breit–Rabi field parameter, which determines the fractions of Rb electronic S momentum that is transferred to rotational angular momentum N and to the ^{129}Xe nuclear spin $K = 1/2$. The fraction of very-short regime vdW interactions is

$$f_{S,i} = \frac{1}{1 + (\omega_{hf,i}\tau)^2}, \tag{21}$$

where $\omega_{hf,i}$ is the ith Rb isotope hyperfine frequency.[36] The F-damping Rb spin destruction rate is

$$\frac{1}{T_{F,i}} = \frac{C_{\alpha\gamma}}{T_{vW,A}} f_{F,i}, \tag{22}$$

where $f_{F,i} = 1 - f_{S,i}$ is the fraction of short regime interactions. Substituting Eqs. (16) and (22) in Eq. (11), we get a full expression

TABLE I. SEOP parameters.

Parameter	Description	Equation/Value	Reference
		Constants	
ω	Spin-rotation frequency of **S** about **N**	$2\pi \times 120$ MHz	38
x	The Breit–Rabi field parameter	3.2	39
η_{85}	Relative abundance of ^{85}Rb	0.7215	…
η_{87}	Relative abundance of ^{87}Rb	0.2785	…
$\omega_{hf,85}$	^{85}Rb hyperfine frequency	$2\pi \times 3.0357$ GHz	36
$\omega_{hf,87}$	^{87}Rb hyperfine frequency	$2\pi \times 6.8347$ GHz	36
		Temperature dependent parameters	
T	Optical cell temperature	353–453 K	This work
K_c	Molecular chemical equilibrium constant	244 Å^3 $(T/373)^{-3/2}$	35
$[G]_{0,Xe}$	Xe characteristic gas density	$\left(\frac{28.3\ \text{Torr}}{760\ \text{Torr}}\right)\cdot\left(\frac{273.15\ \text{K}}{349\ \text{K}}\right)\cdot\left(\frac{349\ \text{K}}{T}\right)^{1/2}$ amg[a]	39–41
$[G]_{0,N_2}$	N_2 characteristic gas density	$\left(\frac{103\ \text{Torr}}{760\ \text{Torr}}\right)\cdot\left(\frac{273.15\ \text{K}}{349\ \text{K}}\right)\cdot\left(\frac{349\ \text{K}}{T}\right)^{1/2}$ amg	39 and 40
$[G]_{0,He}$	He characteristic gas density	$\left(\frac{175\ \text{Torr}}{760\ \text{Torr}}\right)\cdot\left(\frac{273.15\ \text{K}}{358.45\ \text{K}}\right)\cdot\left(\frac{358.45\ \text{K}}{T}\right)^{1/2}$ amg	40 and 42
$[Rb]_{sat}$	Saturation Rb vapor density	$\frac{10^{10.55-\frac{4132\ \text{K}}{T}}}{k_B T}\times 10^{-1}$ m^{-3}	43
		Laser specifications and cell geometry	
P_l	Laser power with cell window transmission losses	160 W	This work
$\lambda_l = c/\nu_l$	Laser center wavelength	794.77 nm	This work
$\Delta\lambda_l = \Delta\nu_l \frac{\lambda_l^2}{c}$	Laser full width at half maximum	0.25 nm	This work
A	Laser and optical cell cross sectional area	4.4×10^{-3} m^3	This work
L_{cell}	Internal cell length	78.7 cm	This work
		Gas mixture composition	
[Xe] : [N_2] : [He]	Gas composition	0.03, 0.1, 0.87	This work
$p = k_B T \sum_j [G]_j$	Gas pressure	1.25 bar	This work
η_K	Enriched ^{129}Xe abundance	0.86	This work
		Rb D_1 line shape	
$\lambda_{D_1} = c/\nu_{D_1}$	Non-shifted Rb D_1 center wavelength	794.77 nm	16
$(\nu_a)_{^4He}$	Rb D_1 line shift due to ^{4}He	4.3 GHz/amg	33
$(\nu_a)_{N_2}$	Rb D_1 line shift due to N_2	−8.25 GHz/amg	33
$(\nu_a)_{Xe}$	Rb D_1 line shift due to Xe	−5.05 GHz/amg	33
$(\Delta\nu_a)_{^4He}$	Rb D_1 linewidth broadening due to ^{4}He	18 GHz/amg	33
$(\Delta\nu_a)_{N_2}$	Rb D_1 linewidth broadening due to N_2	17.8 GHz/amg	33
$(\Delta\nu_a)_{Xe}$	Rb D_1 linewidth broadening due to Xe	18.9 GHz/amg	33
		Rb spin destruction rates	
$\langle\nu\sigma_{SS}\rangle$	Rb-Rb binary spin-destruction rate	4.2×10^{-19} m^{3}s^{-1}	44
$\langle\nu\sigma_{NS}\rangle_{Xe} + \eta_K\langle\nu\sigma_{KS}\rangle$	Rb-Xe binary spin-destruction rate	$8.44\times10^{-21}(T/393\ \text{K})^{1.17}$ m^{3}s^{-1}	45
$\langle\nu\sigma_{NS}\rangle_{N_2}$	Rb-N_2 binary spin-destruction rate	$7.89\times10^{-24}\ (T/393\ \text{K})^3$ m^{3}s^{-1}	46
$\langle\nu\sigma_{NS}\rangle_{^4He}$	Rb-He binary spin-destruction rate	$1.13\times10^{-24}\ (T/393\ \text{K})^{4.26}$ m^{3}s^{-1}	44
		^{129}Xe spin-exchange and spin-destruction rates	
$\langle\sigma v\rangle_{SE}$	Binary ^{129}Xe-Rb spin-exchange cross section	4.02×10^{-22} m^{3}s^{-1}	47
Γ'	Xe relaxation rate in the absence of Rb	1/2640 s^{-1}	16

[a]1 amagat (amg) is the number of ideal gas molecules at standard temperature ($T_0 = 0\,^\circ$C) and pressure ($p_0 = 1$ atm). This is equivalent to 2.687×10^{25} atoms m^{-3}, which is known as the Loschmidt constant.

for Rb spin-destruction due to vdW molecules,

$$\Gamma_{SD}^{vdW}(P_{Rb}) = \sum_i \eta_i \left[\frac{1}{T_{S,i}^{vdW}} + \frac{\nu_i(P_{Rb})}{T_{F,i}}\right] = \frac{C_{\alpha\gamma}}{T_{vW,A}} \sum_i \eta_i [f_{S,i} + \nu_i(P_{Rb}) f_{F,i}] = \frac{C_{\alpha\gamma}}{T_{vW,A}} \sum_i \eta_i [f_{S,i} + \nu_i(P_{Rb})(1 - f_{S,i})]. \quad (23)$$

B. Rb-^{129}Xe spin exchange

Similar to the Rb spin-destruction rate, the Rb to ^{129}Xe spin-exchange rate given by,

$$\gamma_{SE}(P_{Rb}) = \gamma_{SE}^{bc} + \gamma_{SE}^{vdW}(P_{Rb}), \quad (24)$$

has contributions from S-damping binary collisions and the formation and breakup of RbXe vdW molecules, with S-damping and F-damping contributions,

$$\gamma_{SE}^{bc} = \langle \sigma v \rangle_{SE}[Rb], \quad (25)$$

where $\langle \sigma v \rangle_{SE}$ is the binary ^{129}Xe-Rb spin-exchange cross section. The contribution to spin exchange from vdW interactions can be described by[34,37]

$$\gamma_{SE}^{vdW}(P_{Rb}) = \frac{\phi_\alpha^2}{2T_{vW,X}} \sum_i \eta_i [f_{S,i} + \nu_i(P_{Rb}) f_{F,i}] = \gamma'_{vdW}[Rb], \quad (26)$$

where

$$\frac{1}{T_{vW,X}} = \frac{K_c[Rb]}{\tau} \quad (27)$$

is the Rb^{129}Xe molecular formation rate per ^{129}Xe atom.

We can define a total Rb-^{129}Xe spin-exchange cross section as

$$\gamma'(P_{Rb}) = \langle \sigma v \rangle_{SE} + \gamma'_{vdW}(P_{Rb}). \quad (28)$$

Spin-exchange parameter values are given in Table I.

Previous simulation work has frequently omitted the vdW S-damping contribution (i.e., $f_{S,85} = f_{S,87} = 0$) and/or assumed $P_{Rb} = 0$ for the vdW F-damping contribution.[16,20,21,23] By removing these assumptions, the model can be used for SEOP setups of any gas composition and density, enabling broader applicability. For the conditions simulated in this work, adjusting $P_{Rb} = 0$ to $P_{Rb} = 0.8$ leads to a 40% decrease in both Γ_{SD}^{vdW} and γ_{SE}^{vdW}. Furthermore, increasing $f_{S,85}$ and $f_{S,87}$ from zero to their maximum values in this study ($f_{S,85} = 0.0635$ and $f_{S,87} = 0.0132$) leads to an 18% increase in Γ_{SD}^{vdW} and γ_{SE}^{vdW}.

The analytical solution for P_{Xe} buildup is

$$P_{Xe} = \langle P_{Rb} \rangle \frac{\langle \gamma_{SE} \rangle}{\langle \gamma_{SE} \rangle + \Gamma'} \left[1 - \exp\left(\frac{-t_{res}}{\tau_{up}}\right)\right], \quad (29)$$

where $\langle P_{Rb} \rangle$ is the average P_{Rb} over the Rb vapor sample and t_{res} is the residency time of Xe in the cell. $\tau_{up} = (\langle \gamma_{SE} \rangle + \Gamma')^{-1}$ is the spin-up time, where Γ' is the ^{129}Xe relaxation rate in the absence of Rb.

In practice, gas flow, thermodynamics, and photon attenuation may lead to spatial variability of parameters, for which steady-state P_{Xe} buildup must be described by the time-independent convection-diffusion partial differential equation, which is

$$\nabla \cdot (-\mathbf{D}_{Xe} \cdot \nabla \mathbf{P}_{Xe}) + \mathbf{v} \cdot \nabla \mathbf{P}_{Xe} = \gamma_{SE} \cdot \mathbf{P}_{Rb} - (\gamma_{SE} + \mathbf{\Gamma}') \cdot \mathbf{P}_{Xe}, \quad (30)$$

where $\mathbf{D}_{Xe}$ is the Xe diffusion coefficient and $\mathbf{v}$ is the gas velocity. Equation (30) must be solved numerically. The second-order term $\nabla \cdot (-\mathbf{D}_{Xe} \cdot \nabla \mathbf{P}_{Xe})$ cannot be easily solved without the use of finite-element analysis. At high mass flow rate (Q), we also expect $\mathbf{v} \cdot \nabla \mathbf{P}_{Xe} \gg \nabla \cdot (-\mathbf{D}_{Xe} \cdot \nabla \mathbf{P}_{Xe})$, and so this term was excluded in calculations of Eq. (30). We investigated the validity of excluding this term under static gas flow, where $\mathbf{v} \approx 0$, in this work.

C. HP-^{129}Xe production rate

The HP-^{129}Xe production rate can be quantified using the critical flow rate (Q_c), which is the value of Q at which $t_{res} = \tau_{up}$ occurs,[21] i.e.,

$$Q_c = \frac{t_{res} Q}{\tau_{up}}. \quad (31)$$

Q_c was determined by rearranging Eq. (29), which gives

$$Q_c = -Q \log\left(1 - \frac{P_{Xe}(Q)}{P_{Xe}^{eq}}\right), \quad (32)$$

where $P_{Xe}^{eq} = \langle P_{Rb} \rangle \frac{\langle \gamma_{SE} \rangle}{\langle \gamma_{SE} \rangle + \Gamma'}$ is the equilibrium, or static gas flow, P_{Xe}.

Equation (32) is derived from the analytical solution; however, an equivalent Q_c expression for the numerical equation cannot be easily derived from Eq. (30). Instead, we define P_{Xe}^{eq} at the cell outlet, such that $P_{Xe}^{eq} = P_{Rb}(z = 0) \frac{\gamma_{SE}(z=0)}{\gamma_{SE}(z=0) + \Gamma'}$.

III. METHODS

The model framework outlined in Sec. II was implemented in MATLAB (MathWorks) in three distinct ways: (i) to compare photon flux and optical pumping rate attenuation models; (ii) to evaluate numerical vs analytical P_{Xe} buildup models, and (iii) to assess the impact of [Rb] heterogeneity on modeled P_{Xe} and Q_c values. In this work where numerical equations were evaluated, Euler's first-order method was used. Also, Eqs. (1) and (11) show that P_{Rb} and Γ_{SD} form a circular variable dependency, which is difficult to simulate. Therefore, a fixed high P_{Rb} regime ($P_{Rb} = 0.8$) for computing Γ_{SD} was used across simulations, as the most significant spin-exchange interactions occur in high P_{Rb} regions. For the conditions simulated in this work, from $P_{Rb} = 0.5$ to $P_{Rb} = 1$, Γ_{SD} decreases by $\leq 12\%$.

A. Comparing photon flux and optical pumping rate attenuation models

The simplified optical pumping rate attenuation described by Eq. (9) (R model) was simulated and compared with simulations using the full photon flux attenuation model [Φ model: Eq. (5)]. This was performed for two different r values, which is the relative atomic linewidth of the atomic absorption line to the laser spectral output. The values of Φ [Φ model: Eq. (5), R model: Eq. (7)], R [Φ model: Eq. (2), R model: Eq. (9)], and P_{Rb} [Eq. (1) for both models] were computed in this comparison.

B. Numerical vs analytical P_{Xe} buildup models

A summary of the differences between the numerical and analytical P_{Xe} buildup models is given in Table II. The differences in the numerical and analytical P_{Xe} buildup models stem from differing assumptions regarding gas flow within the optical cell. The numerical model, given by Eq. (30), assumes Xe enters the optical cell via the back cell window and travels with plug flow ($\mathbf{v} = -v_z$) toward the front cell window where it is extracted, as shown in Fig. 1(ai). Diffusion of Rb and Xe is neglected assuming that the diffusion length during the spin-up time, or during the Xe residency time if $\tau_{up} > t_{res}$, is much smaller than the cell length, $L_D\left(t = \min\left(\tau_{up}, t_{res}\right)\right) \ll L_{cell}$. [Rb] is assumed to be stationary; thus, the spatial variation in SEOP parameters such as [Rb] and P_{Rb} is considered.

Conversely, the analytical model, described by Eq. (29), assumes rapid diffusion where $L_D\left(t = \min\left(\tau_{up}, t_{res}\right)\right) \gg L_{cell}$. Consequently, within the smaller time scale of τ_{up} or t_{res}, Xe nuclei move through the entire optical cell L_{cell}, illustrated in Fig. 1(aii). This results in a cell-averaged effect of SEOP parameters, disregarding their spatial distribution. Alternatively, this scenario can arise in the presence of convection due to significant temperature gradients, altering $\mathbf{v}$.[24,29]

Simulations were performed for a range of cell temperatures (T) and corresponding $\delta\Phi$ and Q. The absolute percentage difference between P_{Xe} and Q_c calculated by each model was determined ($|\%\text{diff}| = \left(|n_{\text{numerical}} - n_{\text{analytical}}|\right)/\left(n_{\text{numerical}} + n_{\text{analytical}}\right) \times 200\%$) for P_{Xe} and Q_c. $L_D\left(t = \tau_{up}\right)/L_{cell}$ was also calculated to assess the validity of this assumption used to choose models over a wide range of conditions, utilizing the 1D diffusion length ($L_D\left(t = \tau_{up}\right) = \sqrt{2D_{Xe}\tau_{up}}$) for $r_{cell} \ll L_{cell}$. See Appendix for calculation of D_{Xe}.

C. Modeling [Rb] heterogeneity

[Rb] heterogeneity in this 1D simulation framework was modeled by assuming two optical cell regions: one region within a length L_{Rb} from the front of the cell where $[\text{Rb}] = [\text{Rb}]_{sat}$ exists and the region in the remaining portion of the cell where $[\text{Rb}] = 0$, i.e.,

$$[\text{Rb}](z) = \begin{cases} [\text{Rb}]_{sat} & 0 \le z \le L_{Rb}, \\ 0 & L_{Rb} < z \le L_{cell}. \end{cases} \tag{33}$$

This is the worst-case scenario of [Rb] heterogeneity and is shown in Fig. 1(bii), where [Rb] heterogeneity increases with decreasing L_{Rb}. For the numerical model, as SEOP will not occur in the $[\text{Rb}] = 0$ volume, the effective cell length is reduced to just the L_{Rb} region. The effective reduction in cell length also reduces t_{res}. For the analytical model, the assumption of total gas mixing allows [Rb] to be considered homogenized, with a lowering of the cell-averaged Rb density ($\langle[\text{Rb}]\rangle$) by a factor L_{Rb}/L_{cell}.

Scenarios where the region of $[\text{Rb}] = [\text{Rb}]_{sat}$ exists at the back of the cell as opposed to the front of the cell were not simulated. Both cases can be considered identical if depolarization in the $[\text{Rb}] = 0$ region is minimal, i.e., $\Gamma' t_{res}^{[\text{Rb}]=0} \approx 0$, where $t_{res}^{[\text{Rb}]=0}$ is the Xe residency time in the area of $[\text{Rb}] = 0$. This may not be true for rapid Γ', or slow Q and high [Rb] heterogeneity leading to an increase in $t_{res}^{[\text{Rb}]=0}$. For the greatest [Rb] heterogeneity simulated in this work ($L_{Rb} = L_{cell}/8$), $t_{res}^{[\text{Rb}]=0} = 1/\Gamma'$ for volumetric flow rates of 69 cm^3/min, equivalent to $Q = 0.064$ NLPM[48] at 1.25 bar and 120 °C.

Perfect [Rb] homogeneity, $L_{Rb} = L_{cell}$, and three levels of [Rb] heterogeneity, corresponding to three L_{Rb} values, were simulated. $\langle[\text{Rb}]\rangle$, P_{Xe}, and Q_c were calculated for different temperatures and corresponding $\delta\Phi$, for fixed $Q = 2$ NLPM. P_{Xe} and Q_c were determined using both the numerical and the analytical models.

TABLE II. Numerical vs analytical P_{Xe} buildup models.

	Numerical model		Analytical model	
Model	Method	Equation	Method	Equation
Photon attenuation	Same for both models	Eq. (5)	Same for both models	Eq. (5)
Optical pumping	Same for both models	Eq. (2)	Same for both models	Eq. (2)
P_{Rb}	Spatially dependent	Eq. (1)	Cell-averaged	Mean of Eq. (1) over the cell
Static P_{Xe}	Evaluated at $z = 0$	$P_{Rb}(z=0)\dfrac{\gamma_{SE}(z=0)}{\gamma_{SE}(z=0)+\Gamma'}$	Cell-averaged	$\langle P_{Rb}\rangle \dfrac{\langle\gamma_{SE}\rangle}{\langle\gamma_{SE}\rangle+\Gamma'}$
P_{Xe} buildup	Partial differential equation	Eq. (30)	Exponential buildup equation	Eq. (29)
Gas flow	Plug flow	$\mathbf{v} = -v_z$	Complete gas mixing	$L_D\,(t = \min(\tau_{up}, t_{res})) \gg L_{cell}$
Diffusion	Neglected	$L_D\,(t = \min(\tau_{up}, t_{res})) \ll L_{cell}$	Very fast diffusion	$L_D\,(t = \min(\tau_{up}, t_{res})) \gg L_{cell}$

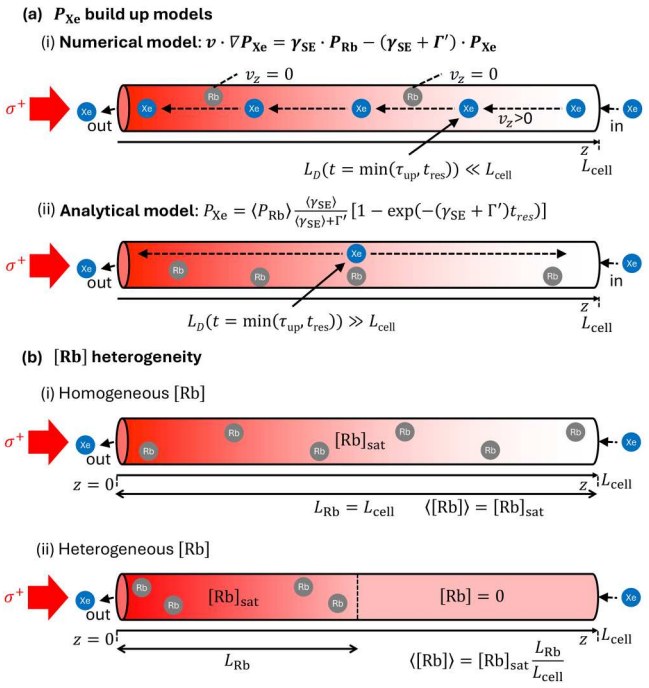

FIG. 1. (a) Diagram showing the differences between the (i) numerical and (ii) analytical ^{129}Xe polarization (P_{Xe}) buildup models. (b) Simulated Rb density ([Rb]) distributions. (i) Homogeneous [Rb] across the full cell length $L_{Rb} = L_{cell}$. (ii) Heterogeneous [Rb] where $[Rb] = [Rb]_{sat}$ only within the L_{Rb} region. Beyond this region $[Rb] = 0$. For the numerical model, this results in a reduction in the effective cell length, whereas for the analytical model, the cell-averaged Rb density, $\langle [Rb] \rangle$ changes by a factor L_{Rb}/L_{cell} compared to the homogeneous case in (a). The red shading in the cells represents photon flux attenuation.

D. Limitations of modeling and phenomena not modeled

Phenomena not modeled are discussed below: (i) Rb cluster formation,[21] as this has not been directly measured yet in optical cells; (ii) radiation trapping,[23] due to the high N_2 partial pressure[32,49,50] ($[N_2] \geq 0.07$ amg, branching ratio $<5\%$); (iii) skewed light effects;[51] (iv) imperfect photon polarization;[34] and (v) the effects of circular dichroism,[52,53] which lead to lower photon efficiency, were also not considered.

The limitations of 1D models compared to 3D models are they neglect convection. Convection will alter **v**, which will depend on cell orientation[23,24] and temperature gradients within the cell. As temperature gradients were not modeled in this work, convection was thus neglected.

IV. RESULTS AND DISCUSSION

A. Photon and optical pumping rate attenuation

When $r = 1$, there is near perfect overlap between the atomic absorption line and the laser spectral output, leading to attenuation of photon flux across all frequencies [Fig. 2(a)]. Conversely, when $r = 0.127$, as observed in our work for $T = 130\,^{\circ}\mathrm{C}$ (For $95\,^{\circ}\mathrm{C} \leq T \leq 180\,^{\circ}\mathrm{C}$, $0.1128 \leq r \leq 0.1388$), the atomic absorption line is smaller than the laser spectral output. In this case, the center of the photon flux spectrum is more attenuated, while the fringes remain weakly attenuated [Fig. 2(b)]. When $r = 1$, both models produce similar values of Φ, R, and P_{Rb}, however, as r decreases, the values produced by each model begin to diverge. The simplified model overestimates R [Fig. 2(d)] leading to higher initial P_{Rb} and a steeper decline compared to the full Φ attenuation model [Fig. 2(e)]. Therefore, under the conditions in this work, the assumption of R being directly proportional to Φ as described in Eq. (7) does not hold. Hence, the full photon flux attenuation model [Eq. (5)] was used throughout this work to most accurately describe optical pumping attenuation.

B. Comparison of P_{Xe} buildup models

Figures 3(ci) and 3(cii) show that P_{Xe} and Q_c values produced by the numerical and analytical models agree ($|\%\mathrm{diff}| < 10\%$) at low to moderate $\delta\Phi$ ($\delta\Phi \leq 66\%$) and high Q values ($Q \geq 0.85$ NLPM). Disagreement is greatest at low Q ($Q \leq 0.15$ NLPM) and high $\delta\Phi$ ($\delta\Phi \geq 83\%$). The deviation in models occurs when $\tau_{up} < t_{res}$, which is at high $\delta\Phi$, where τ_{up} is short, and low Q, where t_{res} is long. Under these conditions, $1 - \exp(-t_{res}/\tau_{up}) \sim 1$ [Eq. (29)], so P_{Xe} buildup in both models is predominantly defined by the P_{Rb} distribution, which increasingly differs between each model as $\delta\Phi$ approaches 100% [Figs. 3(diii) and 3(div)]. The inverse sigmoid shape of the P_{Rb} distribution arises from mismatched laser flux and Rb D_1 absorption line shapes. Precise matching would result in a steeper curve, aligning analytical and numerical models more closely up to the optimal $\delta\Phi$, as observed in Fig. 2.

Conversely, the models agree when $\tau_{up} > t_{res}$, as $1 - \exp(-t_{res}/\tau_{up}) \ll 1$ and P_{Rb} is homogeneous across the cell [Figs. 3(di) and 3(dii)]; however, this is not the optimal regime for high P_{Xe} and rapid HP-^{129}Xe production predicted by either model, as shown in Figs. 3(a) and 3(b). Figure 3(ai) indicates $\delta\Phi \sim 100\%$ for maximum P_{Xe} across $0 \leq Q \leq 2$ NLPM in the numerical model, while Fig. 3(aii) suggests a gradual increase in optimal $\delta\Phi$ with increasing Q in the analytical model. Optimal $\delta\Phi$ for maximum Q_c differs between models, with the analytical model predicting $\delta\Phi = 100\%$ for all Q values [Fig. 3(bii)] whereas the numerical model predicts an increase in optimal $\delta\Phi$ with increasing Q [Fig. 3(bi)]. Hence, model selection is important for optimization efforts.

Where models differ, the numerical model always predicts higher P_{Xe} and lower Q_c values than the analytical model, due to $P_{Rb}(z = 0) > \langle P_{Rb} \rangle$. In the case of extreme P_{Rb} heterogeneity [Fig. 3(dv)] at $\delta\Phi \sim 100\%$, there is an effective reduction in t_{res}, similar to [Rb] heterogeneity. For P_{Xe} buildup, this is compensated somewhat by high [Rb] resulting in rapid γ_{SE} in the high P_{Rb} region toward the front of cell, and P_{Xe} at the front of the cell is still high. This contrasts with the analytical model, where the large $P_{Rb} \sim 0$ region leads to low $\langle P_{Rb} \rangle$, and $\langle P_{Rb} \rangle \sim P_{Xe}$, and no effective reduction in t_{res}. This suggests that faster flow rate regimes where bulk gas flow is the main transport mechanism and diffusion and convection are less significant, i.e., conditions that favor long

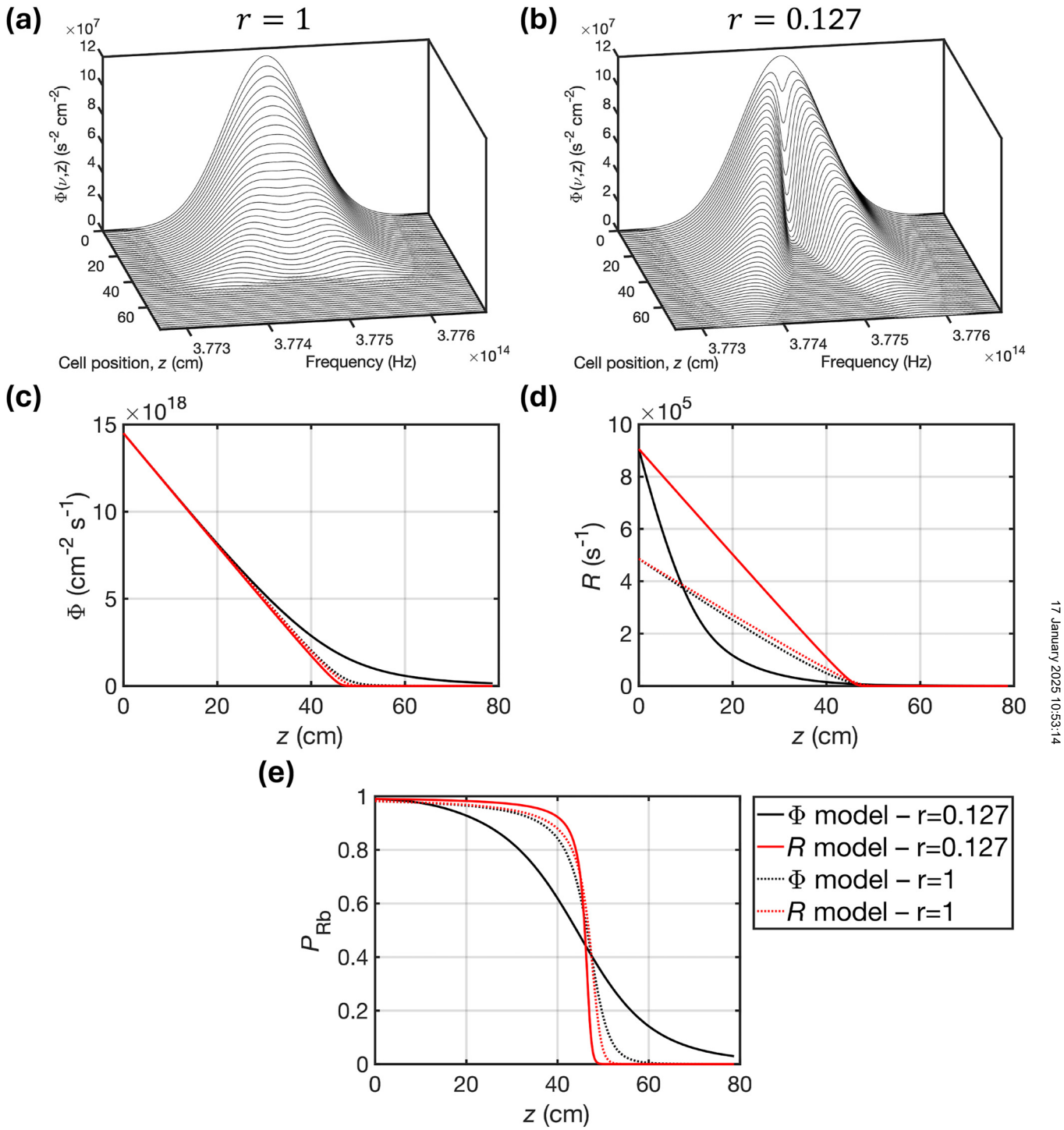

FIG. 2. Photon flux attenuation for (a) $r = 1$ and (b) $r = 0.127$. The optical pumping attenuation and photon flux attenuation models for two different values of r. Cell position (z) dependence of (c) photon flux (Φ), (d) optical pumping rate (R), and (e) Rb polarization (P_{Rb}). $\Gamma_{SD} = 9100\,s^{-1}$, $[Rb] = 3.59 \times 10^{19}\,m^{-3}$, $\Phi(0) = 1.45 \times 10^{19}\,cm^{-2}s^{-1}$, $s = 0$, $\lambda_{D_1} = \lambda_l = 794.77$ nm, and $\Delta\lambda_l = 0.25$ nm were used, corresponding to those for $T = 130\,^{\circ}C$. (c)–(e) show that Φ, R, and P_{Rb} values are similar for both models when $r = 1$; however, they differ when $r = 0.127$.

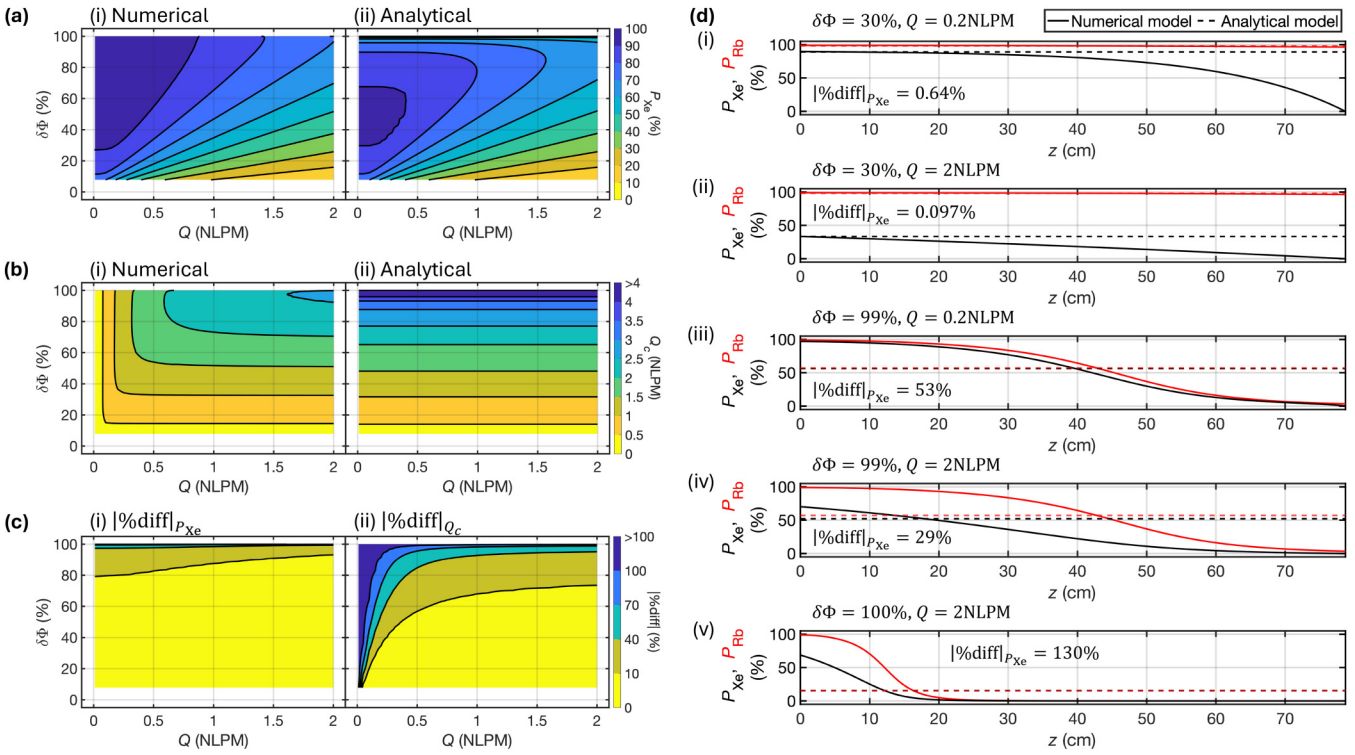

FIG. 3. Contours of laser absorption ($\delta\Phi$) vs flow rate (Q) vs (a) Xe polarization (P_{Xe}) and (b) critical flow rate (Q_c). This was performed for [(ai) and (bi)] the numerical and [(aii) and (bii)] the analytical P_{Xe} buildup models. (c) The absolute percentage difference between the models (|%diff|) was determined for (ci) P_{Xe} values ($|\%\text{diff}|_{P_{Xe}}$) and (cii) Q_c values ($|\%\text{diff}|_{Q_c}$). (c) shows that the models give differing P_{Xe} and Q_c values at low Q and/or high $\delta\Phi$. (d) P_{Xe}, P_{Rb}, and $\delta\Phi$ vs cell position (z) using the numerical (solid lines) and analytical (dashed lines) models for different $\delta\Phi$ and Q values. (di) and (dii) at low $\delta\Phi$ show agreement in $P_{Xe}(z=0)$ between models, while (diii)–(dv) at high $\delta\Phi$ show disagreement, due to heterogeneous P_{Rb} distributions. N.B.: dashed lines in (dv) are overlapping.

optical cells over small optical cells, will lead to higher output P_{Xe}. This supports the use of large optical cells over small optical cells in CF-SEOP polarizers.

For static gas flow conditions ($\mathbf{v} \approx 0$), where the numerical and analytical models differ, $L_D(t = \tau_{up})$ was evaluated to determine the validity of neglecting the second-order term in Eq. (30). In our work, where $|\%\text{diff}|_{P_{Xe}}(Q = 0.01\,\text{NLPM}) \geq 10\%$, the range $0.11 \geq L_D(t = \tau_{up})/L_{cell} \geq 0.025$ indicates that the second-order term in Eq. (30) can be neglected. This finding also suggests, under these conditions, the numerical model more accurately describes P_{Xe} buildup than the analytical model due to $L_D(t = \tau_{up}) \ll L_{cell}$. However, the precise threshold value of $L_D(t = \tau_{up})/L_{cell}$ at which gas mixing across the entire cell length occurs has not been determined. It is likely that an intermediate regime exists where only partial local gas mixing occurs over a portion of the cell. Under these conditions, incorporating the second-order diffusion term in Eq. (30) may provide a more accurate representation of P_{Xe} buildup.

For previous studies in which the analytical model was used, polarizers were operated at low $\delta\Phi$ and moderate $L_D(t = \tau_{up})/L_{cell}$ values were demonstrated, suggesting that the use of the analytical model is valid in those contexts. Notable examples include the previous generation Sheffield polarizer[20] [$0.11 \leq L_D(t = \min(\tau_{up}, t_{res}))/L_{cell} \leq 0.19$, $\delta\Phi = 43\%$] as well as batch-mode polarizers developed by Nikolaou and colleagues [$L_D(t = \min(\tau_{up}, t_{res}))/L_{cell} = 0.28$, $\delta\Phi \sim 53\%$] for Ref. 11 and [$L_D(t = \tau_{up})/L_{cell} = 0.41$, $\delta\Phi$ not reported] for Ref. 13.

Modeled values were compared with measurements acquired on the previous generation Sheffield polarizer, using re-simulated conditions of $P_l = 133$ W and $\Delta\lambda_l = 0.3$ nm.[16] At $\delta\Phi = 87.5\%$, $Q_c = 2.527$ NLPM[54] was under-estimated by the numerical model ($Q_c = 2.00$ NLPM) and overestimated by the analytical model ($Q_c = 2.84$ NLPM). Both models also overestimated $P_{Xe}(Q = 2\text{NLPM})$ by factor-1.8 (analytical model) and 2 (numerical model). Lower-than-saturation [Rb] may contribute to the model-measurement discrepancies.[17,29] From Ref. 16, [Rb] can be estimated using measured values $\tau_{up} = 71$ s, $\gamma' = 1.63 \times 10^{-21}$ m^3 s^{-1}, and $1/\Gamma' = 44$ min as $[\text{Rb}] = (\tau_{up}^{-1} - \Gamma')/\gamma' = 8.4 \times 10^{18}$ m^{-3} $= 0.31[\text{Rb}]_{sat}$. Substituting this [Rb] into both models improved P_{Xe} agreement (factor-1.3 difference for both models) but underpredicted Q_c [factor-2.1 (analytical) and 2.2 (numerical)] and $\delta\Phi$ (factor-1.8 in both models). Q_c (or τ_{up}) discrepancy has been suggested to be due to higher-than-predicted γ'[30] [Eq. (28)]. Temperature-dependent Γ' observed in studies of both ^{3}He-Rb[55] and ^{129}Xe-Rb[56] SEOP may also contribute. $\delta\Phi$ discrepancies are largely unreported in clinical-scale CF polarizers,

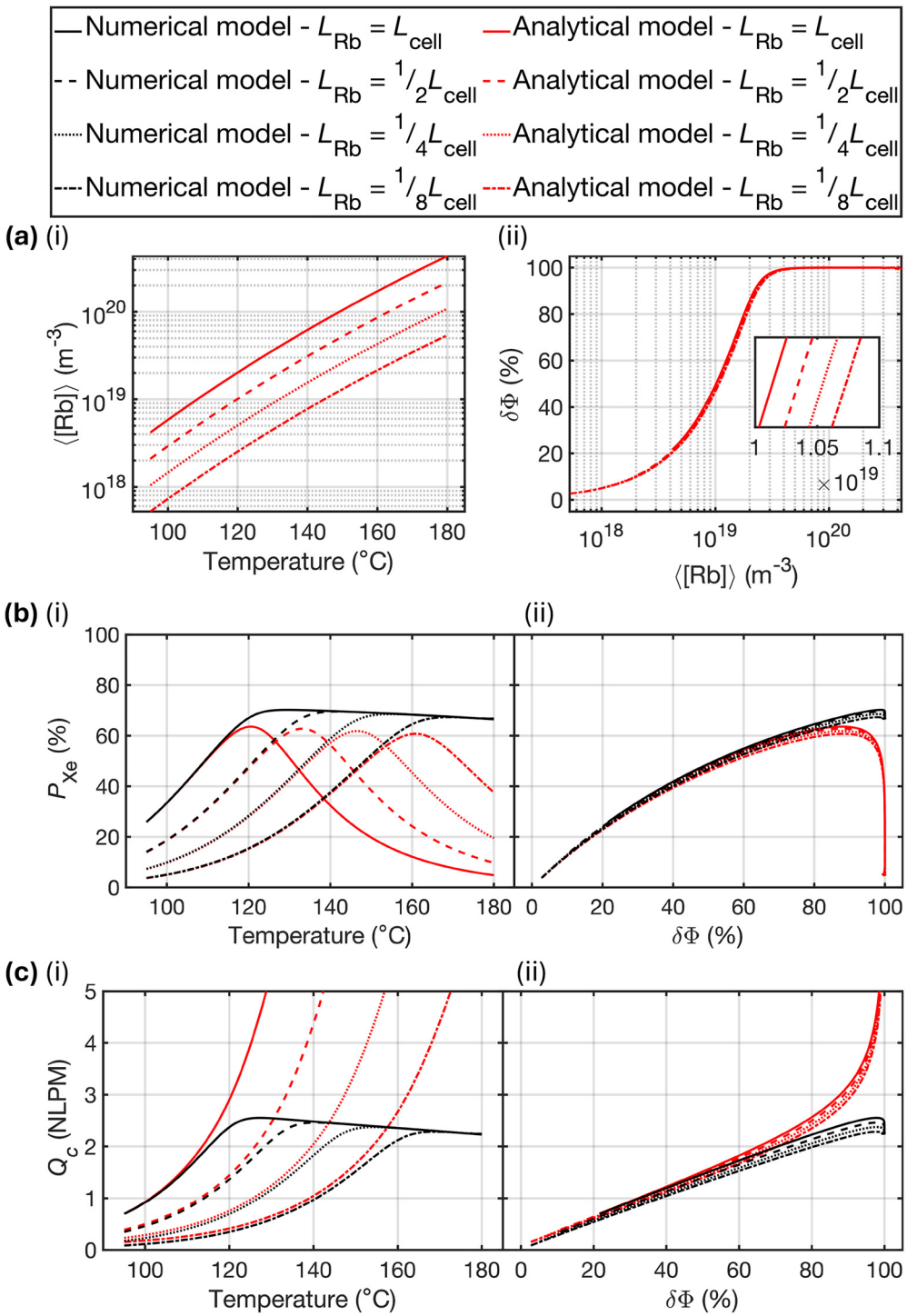

FIG. 4. (ai) Cell-averaged Rb density ($\langle[Rb]\rangle$) vs temperature and (aii) $\delta\Phi$ vs $\langle[Rb]\rangle$ for different L_{Rb}. (b) P_{Xe} and (c) Q_c vs (i) temperature and (ii) $\delta\Phi$. $L_{Rb} = L_{cell}$ (solid lines), $L_{Rb} = L_{cell}/2$ (dashed lines), $L_{Rb} = L_{cell}/4$ (dotted lines) and $L_{Rb} = L_{cell}/8$ (dash-dotted lines) correspond to increasing [Rb] heterogeneity [Eq. (33)]. Black and red lines indicate the numerical model and analytical models, respectively. (b) and (c) show that the optimal temperature for maximum P_{Xe} and Q_c greatly differs across varying levels of [Rb] heterogeneity, while the optimal $\delta\Phi$ value remains fairly consistent.

which makes further comparisons of measurements to modeled values not possible. Inclusion of additional optical pumping limiting factors, discussed in Sec. III D, should be investigated in future work. Comparisons between existing experimental measurements and modeled values, particularly for high flow rate, large optical cell CF-polarizers similar to the Sheffield polarizer modeled here, are complicated by the lack of consistent and precise measurements of SEOP parameters under identical polarizer conditions. Systematic variability across polarizers stems from factors such as increases in optical cell surface relaxation rate over time,[57] optical pumping laser broadening and power degradation, changes to the Rb source distribution,[29] and thermal regulation issues.[31] To address these issues, future experiments should involve simultaneous measurement of multiple SEOP parameters, as well as spatially resolved measurements across the optical cell. Such efforts would enable a more comprehensive understanding of the discrepancies between experimental data and model predictions.

C. [Rb] heterogeneity

Figure 4(ai) shows variations in $\langle[\mathrm{Rb}]\rangle$ with temperature for different levels of [Rb] heterogeneity, as expected. This corresponded to greatly varying optimal temperatures for maximum P_{Xe}, as depicted in Fig. 4(bi), and Q_c values, shown in Fig. 4(ci). The $\delta\Phi$ dependence of $\langle[\mathrm{Rb}]\rangle$ [Fig. 4(aii)], P_{Xe} [Fig. 4(bii)], and Q_c [Fig. 4(cii)] are mostly unaffected by the level of [Rb] heterogeneity, irrespective of the P_{Xe} model used. Therefore, optimal $\delta\Phi$ is a more robust parameter for optimization efforts as well as model-experiment comparisons compared to optimal temperature. In addition, this shows that optimal $\langle[\mathrm{Rb}]\rangle$ level is more significant than [Rb] homogeneity for P_{Xe} buildup. On the surface, this appears to discount efforts to improve [Rb] homogeneity; however, simulations indicate a slight increase in maximum P_{Xe} and lower optimal temperature with increasing [Rb] homogeneity, as shown in Fig. 4(bi). This is desirable for reducing thermal regulation demands and the potential use of anti-relaxation surface coatings, which have been shown to reduce Γ'[58,59] but react with Rb at $\gtrsim 170\,^{\circ}\mathrm{C}$.[59,60]

V. CONCLUSIONS AND FUTURE WORK

In this work, a revised SEOP modeling framework was used to assess the applicability of modeling approaches to large optical cell CF-SEOP polarizers. Commonly used analytical and numerical P_{Xe} buildup models were shown to give diverging P_{Xe} and Q_c values at low Q and high $\delta\Phi$. This divergence may contribute to observed discrepancies between theoretical and experimental production rates. Theoretical and experimental P_{Xe} discrepancies are likely not solely due to the choice of model however, as significantly different laser absorption values between theory and experiments suggest an incomplete optical pumping model. In addition, [Rb] heterogeneity was shown to have a minimal effect on optimal $\delta\Phi$ and a small detrimental impact on P_{Xe} values. However, optimal temperatures were significantly increased with high levels of [Rb] heterogeneity, which is undesirable for thermal management and the application of anti-relaxation surface coatings. The updated simulation framework presented in this work can be applied to model other SEOP systems, to aid optimization of running conditions, and should therefore be of interest to researchers working in this field. MATLAB functions for modeling are available in the supplementary material.

SUPPLEMENTARY MATERIAL

See the supplementary material for the MATLAB function of the 1D model presented in this work (SEOP_1D.m), an additional MATLAB function required for this to run (erfz.m),[61] and the MATLAB function that calculates the Xe diffusion coefficient (diffusion_coefficient.m).

ACKNOWLEDGMENTS

The authors thank Ho-Fung Chan for useful discussions about calculating the xenon diffusion coefficient and Neil Stewart for helpful manuscript revisions. This work was supported by an Academy of Medical Sciences Springboard award grant, the Medical Research Council under Grant No. MR/M008894/1; and the Engineering and Physical Sciences Research Council under Grant No. EP/X025187/1.

AUTHOR DECLARATIONS

Conflict of Interest

The authors have no conflicts to disclose.

Author Contributions

J. E. Ball: Conceptualization (equal); Data curation (equal); Formal analysis (equal); Investigation (equal); Methodology (equal); Software (equal); Writing – original draft (equal); Writing – review & editing (equal). **J. M. Wild:** Funding acquisition (equal); Project administration (equal); Resources (equal); Supervision (supporting); Writing – review & editing (equal). **G. Norquay:** Conceptualization (equal); Formal analysis (equal); Funding acquisition (equal); Methodology (equal); Project administration (equal); Resources (equal); Software (equal); Supervision (equal); Writing – review & editing (equal).

DATA AVAILABILITY

The data that support the findings of this study are available from the corresponding author upon reasonable request.

APPENDIX: Xe DIFFUSION

The mutual diffusion coefficient of Xe and gas species β is calculated as[62]

$$D_{\mathrm{Xe}\beta} = \frac{3f_D}{8p\sigma_{\mathrm{Xe}\beta}^2\Omega_{\mathrm{Xe}\beta}}\sqrt{\frac{(k_BT)^3}{\pi}\left(\frac{M_{\mathrm{Xe}}+M_\beta}{2M_{\mathrm{Xe}}M_\beta}\right)}, \tag{A1}$$

where M_{Xe} and M_β are the molecular masses of Xe and species β, f_D is a correction factor that accounts for the gas mixture, which can be approximated as $f_D \sim 1$ for most gas mixtures,[62] $\sigma_{\mathrm{Xe}\beta} = 1/2(\sigma_{\mathrm{Xe}} + \sigma_\beta)$ is the characteristic length of the Lennard-Jones potential. $\Omega_{\mathrm{Xe}\beta}$ is the collision integral, which is

TABLE III. Xe diffusion coefficient parameters, given by Ref. 62.

Gas species	σ (Å)	ε/k (K)	M (g/mol)
Xe	4.047	231.0	129.44[a]
N_2	3.798	71.4	28.013
He	2.551	10.22	4.003

[a]Enriched Xe (86% ^{129}Xe).

given by[62–64]

$$\Omega_{\mathrm{Xe}\beta} = \frac{1.06036}{(T^*)^{0.156\,10}} + \frac{0.19300}{\exp(0.47635(T^*))} + \frac{1.03587}{\exp(1.52996(T^*))} + \frac{1.76474}{\exp(3.89411(T^*))}, \tag{A2}$$

where $T^* = kT/\varepsilon_{\mathrm{Xe}\beta}$ and $\varepsilon_{\mathrm{Xe}\beta} = \sqrt{\varepsilon_{\mathrm{Xe}}\varepsilon_\beta}$. $\varepsilon_{\mathrm{Xe}}$ and ε_β are the energy parameters of Xe and species β. Diffusion parameter values are given in Table III.

The observable Xe diffusion coefficient is

$$D_{\mathrm{Xe}} = \left(\sum_{\beta=1}^{n} \frac{x_\beta}{D_{\mathrm{Xe}\beta}}\right)^{-1}, \tag{A3}$$

where x_β is the molar fraction of gas species β and $n = 3$ is the total number of gas species in the mixture.

REFERENCES

[1]J. P. Mugler III and T. A. Altes, J. Magn. Reson. Imaging **37**, 313 (2013).
[2]H. Marshall, N. J. Stewart, H.-F. Chan, M. Rao, G. Norquay, and J. M. Wild, Prog. Nucl. Magn. Reson. Spectrosc. **122**, 42 (2021).
[3]Y. Wang and I. J. Dmochowski, Acc. Chem. Res. **49**, 2179 (2016).
[4]J. Jayapaul and L. Schröder, Molecules **25**, 957 (2020).
[5]V. Batarchuk, Y. Shepelytskyi, V. Grynko, A. H. Kovacs, A. Hodgson, K. Rodriguez, R. Aldossary, T. Talwar, C. Hasselbrink, I. C. Ruset, B. DeBoef, and M. S. Albert, Int. J. Mol. Sci. **25**, 1939 (2024).
[6]E. Weiland, M.-A. Springuel-Huet, A. Nossov, and A. Gédéon, Microporous Mesoporous Mater. **225**, 41 (2016).
[7]W. A. Terrano and M. V. Romalis, Quantum Sci. Technol. **7**, 014001 (2022).
[8]T. G. Walker and W. Happer, Rev. Mod. Phys. **69**, 629 (1997).
[9]M. S. Rosen, T. E. Chupp, K. P. Coulter, R. C. Welsh, and S. D. Swanson, Rev. Sci. Instrum. **70**, 1546 (1999).
[10]B. Driehuys, G. D. Cates, E. Miron, K. Sauer, D. K. Walter, and W. Happer, Appl. Phys. Lett. **69**, 1668 (1996).
[11]P. Nikolaou, A. M. Coffey, L. L. Walkup, B. M. Gust, N. Whiting, H. Newton, S. Barcus, I. Muradyan, M. Dabaghyan, G. D. Moroz, M. S. Rosen, S. Patz, M. J. Barlow, E. Y. Chekmenev, and B. M. Goodson, Proc. Natl. Acad. Sci. **110**, 14150 LP (2013).
[12]J. R. Birchall, R. K. Irwin, P. Nikolaou, A. M. Coffey, B. E. Kidd, M. Murphy, M. Molway, L. B. Bales, K. Ranta, M. J. Barlow, B. M. Goodson, M. S. Rosen, and E. Y. Chekmenev, J. Magn. Reson. **319**, 106813 (2020).
[13]J. R. Birchall, M. R. H. Chowdhury, P. Nikolaou, Y. A. Chekmenev, A. Shcherbakov, M. J. Barlow, B. M. Goodson, and E. Y. Chekmenev, Molecules **27**, 1327 (2022).
[14]I. C. Ruset, S. Ketel, and F. W. Hersman, Phys. Rev. Lett. **96**, 53002 (2006).
[15]G. Schrank, Z. Ma, A. Schoeck, and B. Saam, Phys. Rev. A **80**, 63424 (2009).
[16]G. Norquay, G. J. Collier, M. Rao, N. J. Stewart, and J. M. Wild, Phys. Rev. Lett. **121**, 153201 (2018).
[17]J. W. Plummer, K. Emami, A. Dummer, J. C. Woods, L. L. Walkup, and Z. I. Cleveland, J. Magn. Reson. **320**, 106845 (2020).
[18]C. H. Volk, T. M. Kwon, and J. G. Mark, Phys. Rev. A **21**, 1549 (1980).
[19]W. Happer, E. Miron, S. Schaefer, D. Schreiber, W. A. van Wijngaarden, and X. Zeng, Phys. Rev. A **29**, 3092 (1984).
[20]G. Norquay, S. R. Parnell, X. Xu, J. Parra-Robles, and J. M. Wild, J. Appl. Phys. **113**, 44908 (2013).
[21]M. S. S. Freeman, K. Emami, and B. Driehuys, Phys. Rev. A **90**, 23406 (2014).
[22]I. C. Ruset, "Hyperpolarized ^{129}Xe production and applications," Ph.D. thesis (University of New Hampshire, Durham, 2005).
[23]A. Fink, D. Baumer, and E. Brunner, Phys. Rev. A **72**, 53411 (2005).
[24]A. Fink and E. Brunner, Appl. Phys. B **89**, 65 (2007).
[25]G. M. Schrank, "A novel, finite-element model for spin-exchange optical pumping using an Open-Source Code," arXiv:1911.01574 (2019).
[26]G. M. Schrank, "Fluid and thermal dynamical analysis of three-dimensional spin-exchange optical pumping cells," arXiv:2005.08404 (2020).
[27]S. Appelt, A. Ben-Amar Baranga, A. R. Young, and W. Happer, Phys. Rev. A **59**, 2078 (1999).
[28]S. Appelt, T. Ünlü, K. Zilles, N. J. Shah, S. Baer-Lang, and H. Halling, Appl. Phys. Lett. **75**, 427 (1999).
[29]M. Kelley, A. Burant, and R. T. Branca, J. Appl. Phys. **128**, 144901 (2020).
[30]M. Kelley and R. T. Branca, J. Appl. Phys. **129**, 154901 (2021).
[31]J. E. Ball, J. M. Wild, and G. Norquay, Molecules **28**, 11 (2023).
[32]M. E. Wagshul and T. E. Chupp, Phys. Rev. A **40**, 4447 (1989).
[33]M. V. Romalis, E. Miron, and G. D. Cates, Phys. Rev. A **56**, 4569 (1997).
[34]S. Appelt, A. B.-A. Baranga, C. J. Erickson, M. V. Romalis, A. R. Young, and W. Happer, Phys. Rev. A **58**, 1412 (1998).
[35]T. G. Walker, Phys. Rev. A **40**, 4959 (1989).
[36]I. A. Nelson, "Physics of practical spin-exchange optical pumping," Ph.D. thesis (University of Wisconsin-Madison, Madison, 2001).
[37]T. G. Walker and M. S. Larsen, "Chapter eight: Spin-exchange-pumped NMR gyros," *Advances In Atomic, Molecular, and Optical Physics* (Academic Press, 2016), pp. 373–401.
[38]N. D. Bhaskar, W. Happer, M. Larsson, and X. Zeng, Phys. Rev. Lett. **50**, 105 (1983).
[39]X. Zeng, Z. Wu, T. Call, E. Miron, D. Schreiber, and W. Happer, Phys. Rev. A **31**, 260 (1985).
[40]G. D. Cates, R. J. Fitzgerald, A. S. Barton, P. Bogorad, M. Gatzke, N. R. Newbury, and B. Saam, Phys. Rev. A **45**, 4631 (1992).
[41]M. A. Bouchiat, J. Brossel, and L. C. Pottier, J. Chem. Phys. **56**, 3703 (1972).
[42]N. Ramsey, E. Miron, X. Zeng, and W. Happe, Chem. Phys. Lett. **102**, 340 (1983).
[43]T. J. Killian, Phys. Rev. **27**, 578 (1926).
[44]A. B.-A. Baranga, S. Appelt, C. J. Erickson, A. R. Young, and W. Happer, Phys. Rev. A **58**, 2282 (1998).
[45]I. A. Nelson and T. G. Walker, Phys. Rev. A **65**, 12712 (2001).
[46]W. C. Chen, T. R. Gentile, T. G. Walker, and E. Babcock, Phys. Rev. A **75**, 13416 (2007).
[47]B. Song, Y. Wang, and N. Zhao, Phys. Rev. A **104**, 23105 (2021).
[48]NLPM = nominal liters per minute defined at a reference temperature of 20 °C and a pressure of 1 atm.
[49]E. S. Hrycyshyn and L. Krause, Can. J. Phys. **48**, 2761 (1970).
[50]E. Brunner, Concepts Magn. Reson. **11**, 313 (1999).
[51]B. Chann, E. Babcock, L. W. Anderson, and T. G. Walker, Phys. Rev. A **66**, 33406 (2002).
[52]B. Lancor, E. Babcock, R. Wyllie, and T. G. Walker, Phys. Rev. Lett. **105**, 83003 (2010).
[53]B. Lancor, E. Babcock, R. Wyllie, and T. G. Walker, Phys. Rev. A **82**, 43435 (2010).
[54]Mass flow rates in Ref. 16 are misreported as SCCM (0 °C reference) when they were actually based on 20 °C reference.
[55]E. Babcock, B. Chann, T. G. Walker, W. C. Chen, and T. R. Gentile, Phys. Rev. Lett. **96**, 83003 (2006).

[56]N. Shah, T. Ünlü, H.-P. Wegener, H. Halling, K. Zilles, and S. Appelt, NMR Biomed. **13**, 214 (2000).
[57]M. Repetto, E. Babcock, P. Blümler, W. Heil, S. Karpuk, and K. Tullney, J. Magn. Reson. **252**, 163 (2015).
[58]X. Zeng, E. Miron, W. A. Van Wijngaarden, D. Schreiber, and W. Happer, Phys. Lett. A **96**, 191 (1983).
[59]E. R. Oteiza, "Search for a permanent electric dipole moment in xenon-129 using simultaneous helium-3 magnetometry," Ph.D. thesis (Harvard University, Cambridge, 1992).
[60]S. J. Seltzer and M. V. Romalis, J. Appl. Phys. **106**, 114905 (2009).
[61]P. Godfrey, see https://www.mathworks.com/matlabcentral/fileexchange/3574-erfz for "erfz, MATLAB Central File Exchange" (2024) (accessed August 16, 2024).
[62]B. E. Poling, J. M. Prausnitz, and J. P. O'Connell, *Properties of Gases and Liquids*, 5th ed. (McGraw-Hill Education, New York, 2001).
[63]P. D. Neufeld, A. R. Janzen, and R. A. Aziz, J. Chem. Phys. **57**, 1100 (1972).
[64]T. Pavlin, "Hyperpolarized gas polarimetry and imaging at low magnetic field," Ph.D. thesis (California Institute of Technology, Pasadena, 2003).